Non-uniform aging of cycled commercial LiFePO$_4$//graphite cylindrical cells revealed by *post-mortem* analysis

Matilda Klett [a],[*], Rickard Eriksson [b], Jens Groot [c],[d], Pontus Svens [a],[e], Katarzyna Ciosek Högström [b], Rakel Wreland Lindström [a], Helena Berg [f], Torbjörn Gustafson [b], Göran Lindbergh [a], Kristina Edström [b]

[a] *Applied Electrochemistry, KTH Royal Institute of Technology, SE-10044 Stockholm, Sweden*
[b] *Department of Chemistry, Ångström Laboratory, Uppsala University, Box 538, SE-751 21 Uppsala, Sweden*
[c] *Department of Energy and Environment, Chalmers University of Technology, SE-412 88 Göteborg, Sweden*
[d] *Volvo Group Trucks Technology, SE-405 08 Göteborg, Sweden*
[e] *Scania CV AB, SE-151 87 Södertälje, Sweden*
[f] *AB Libergreen, SE-411 27 Göteborg, Sweden*

HIGHLIGHTS

- *Post-mortem* characterization of commercial cells for hybrid electric vehicles.
- Cycling of cylindrical LiFePO$_4$/graphite cells gives rise to non-uniform aging.
- More severe graphite electrode degradation is observed further into the jellyroll.
- Aging is caused by local loss of cyclable Li and SEI growth at the negative electrode.

ARTICLE INFO

ABSTRACT

Aging of power-optimized commercial 2.3 Ah cylindrical LiFePO$_4$//graphite cells to be used in hybrid electric vehicle is investigated and compared for three different aging procedures; (i) using a simulated hybrid electric vehicle cycle within a narrow SOC-range, (ii) using a constant-current cycle over a 100% SOC-range, and (iii) stored during three years at 22 °C. Postmortem analysis of the cells is performed after full-cell electrochemical characterization and discharge. EIS and capacity measurements are made on different parts of the disassembled cells. Material characterization includes SEM, EDX, HAXPES/XPS and XRD. The most remarkable result is that both cycled cells displayed highly uneven aging primarily of the graphite electrodes, showing large differences between the central parts of the jellyroll compared to the outer parts. The aging variations are identified as differences in capacity and impedance of the graphite electrode, associated with different SEI characteristics. Loss of cyclable lithium is mirrored by a varying degree of lithiation in the positive electrode and electrode slippage. The spatial variation in negative electrode degradation and utilization observed is most likely connected to gradients in temperature and pressure, that can give rise to current density and potential distributions within the jellyroll during cycling.

© 2014 Elsevier B.V. All rights reserved.

1. Introduction

Electrification of vehicles is highly interesting for vehicle manufacturers worldwide in order to reduce CO$_2$ emissions and air pollution [1—3]. However, the high cost of the energy storage system and limited charging infrastructure delay mass production for battery-only electric vehicles [4]. Hybrid electric vehicles (HEV) are in terms of fuel reduction, cost and performance therefore a reliable alternative [5,6]. Various battery chemistries have been of interest for the different vehicle concepts. The rechargeable lithium-ion battery has high energy and power capacity and the commercially available LiFePO$_4$/graphite system is considered safe, environmentally benign, and inexpensive among the different Li-ion battery chemistries [7—9].

The demand on the battery system in a heavy-duty HEV is different compared to a passenger car since buses and distribution

* Corresponding author.
E-mail address: mklett@kth.se (M. Klett).

trucks generally are used between 10 and 15 h per day all year around with high power demands in challenging duty cycles [2,10]. These conditions presumably have negative effects on the durability of the battery system with significant consequences for performance in terms of capacity, power, and safety over time. The challenges for the vehicle manufactures are to find a way to use the battery system under optimal conditions and at the same time save as much fuel as possible.

To understand the underlying causes of how certain driving conditions correlate to performance degradation is challenging but imperative to design sustainable electrified vehicles. Several aging mechanisms in LiFePO$_4$/graphite cells have been established. For commercial cells, loss of cyclable lithium in side reactions leading to capacity fade has been reported as the primary aging effect when stored at elevated temperatures [11–13] and cycled at room and elevated temperatures [13–15]. Also secondary losses, such as loss of graphite active material [13,15–17] and coarsening of particles and porosity decrease at the LiFePO$_4$ electrode [18–20] have been demonstrated upon cycling. Calendar aging has been shown to be more affected by elevated temperature than state-of-charge (SOC) [11].

In the combination of several underlying aging mechanisms, *post-mortem* analysis of aged cells is useful to distinguish between different aging processes occurring at the different components of a cell. With some exceptions, it is mostly performed on small cells and under well-defined conditions to investigate the specific impact of certain cycling conditions or comparing electrolyte/electrode modifications, for example [16,21]. We have previously studied small LiFePO$_4$/graphite pouch cells and investigated the effect of temperature and hybrid cycle aging vs. calendar aging by both material [22] and electrochemical post-analysis combined with physics-based modeling [17]. However, to investigate whether the mechanisms observed at a small scale are relevant for the application, it is important to expand the results from these well-defined model systems, to commercial cells used for vehicles. At this scale and conditions, possible distribution of temperature, current density, and SOC not present in lab-scale cells could impact the long-term performance and utilization of the cell. Heat production (irreversible and reversible) and current distribution are intrinsically connected, as reaction and transport resistances are temperature dependent, and the cell material and design, which dictates the local heat dissipation, affect the possible development of inhomogeneities in the cell [23]. Fleckenstein et al. [24] theoretically evaluated the internal distribution of temperature, current and SOC in a LiFePO$_4$ cylindrical wound cell during charge and discharge pulses showing the increased temperature and current density in the center of the cell. Somasundaram et al. [25], reported instead a negligible temperature distribution calculated for a LiMn$_2$O$_4$ cylindrical cell, but a significant average temperature increase for currents up to 5C in a cylindrical 18650 cell. The effect on current [26] and temperature [27] distributions due to placement of tabs in the cell design has also been reported. With temperature/SOC/current-dependent aging processes, the cell design's influence on distributing these properties could affect overall aging and is therefore important to take into account. It becomes hence relevant to study different parts of the electrodes and separators in the cells after different kinds of aging processes. *Post-mortem* aging studies of medium- to large-scale Li-ion cells designed for automotive use have been reported in literature [12,15,18,28–30] and are carried out within different companies. So far, however, little focus has been on any spatial variations over the cell due to cycling. The importance of a further accounting of aging variation across different length-scales is discussed and demonstrated by Nagpure et al. [19].

For commercial cells, electrochemical techniques such as incremental capacity analysis [31,32], differential voltage analysis [33], and electrochemical impedance spectroscopy (EIS) [34] have proved to be valuable methods to characterize degradation mechanisms. However, although these methods may provide comparably accurate assessments of the general aging in the cells, naturally they cannot reveal differences between different parts of the cell. Furthermore, since the aging mechanisms of Li-ion battery cells are complex [35–37], it is rarely possible to isolate one mechanism at a time in larger cells and test its specific dependence on operating conditions.

In previous work on commercially available 26650 power optimized cylindrical cells containing LiFePO$_4$/graphite, cells were aged according to a variety of load conditions such as current rate, cycle characteristics, SOC range, and temperature [38,39]. In the present work, *post-mortem* analysis is employed to study how certain realistic cycling patterns in commercially available cells affect the interior degradation processes in order to evaluate the relevance of different aging processes in relation to the overall cell performance. Three cells aged by three profoundly different load conditions were chosen: (i) cycling according to real hybrid electric vehicle driving conditions within a narrow SOC-range (HEVC), (ii) a simple constant-current charge–discharge cycle with approximately 90% depth-of-discharge (CCC), and (iii) calendar aged by storage for 3 years at 3.3 V floating potential (CAL). The HEVC represent the realistic scenario for HEV applications and was chosen to mimic a hybrid electric city-bus designed to reduce fuel consumption by recuperating brake energy and avoid idling. The CCC and CAL conditions are chosen as two extreme cases to be used for comparison, representing two relatively common aging conditions when studying battery degradation. Cycling in a wide SOC range, 80–100%, is known to have a profound effect on aging [40,41], while calendar aging in room temperature is only slightly detrimental for cell performance [11] and electrode degradation [17]. The electrode properties where investigated on several locations within the jellyroll with a combination of chemical, electrochemical, and physical methods (XPS, SEM, XRD, EIS, etc.), which serves as a means to examine the impact of surface and morphological changes on electrode performance.

2. Experimental

2.1. Cycling/aging of commercial cells

Commercial power-optimized LiFePO$_4$/graphite cells of 26650 cylindrical format with 2.3 Ah nominal capacity were obtained from the same batch and used in the aging investigation. Three different aging conditions were studied, referred to as HEVC, CCC, and CAL. Duplicate cells where aged according to each load pattern, and one cell from each aging condition was chosen for post-mortem analysis when found to behave reproducibly.

The battery load cycle for the HEVC condition represent a typical hybrid city-bus where the operating conditions are chosen to optimize battery life [42]. This load cycle consists of comparably high currents of up to 23 and 15 C-rates, for discharge and charge, respectively, but a moderate SOC range, as seen in Fig. 1a. The C-rates are based on initial nominal capacity, where 1C is the current to fully charge the battery in 1 h. Three dynamic cycles of approximately 70 min is followed by a potentiostatic/galvanostatic SOC adjustment procedure. The CCC condition is a constant-current constant-voltage (CC–CV) charge and CC discharge cycle between 2.0 and 3.6 V with a cut-off current of 0.57 A. These conditions correspond to cycling the cell approximately between 5% and 95% SOC, often used in cell aging tests. The current rate of 3.75 C (8.63 A) was chosen to give approximately the same capacity throughput per time unit as the HEVC. Even though the measured skin temperature during cycling for the HEVC cell is higher than the CCC cell,
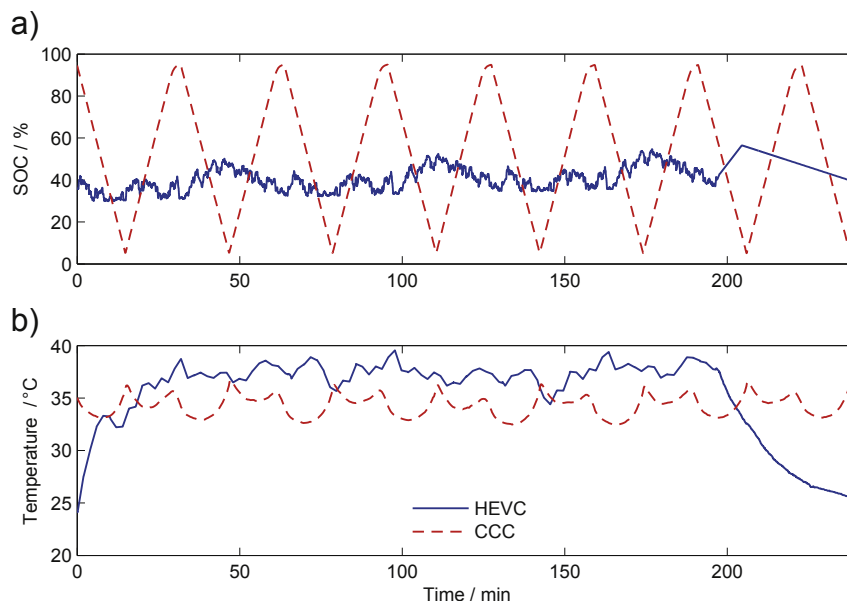
Fig. 1. Cycle characteristics for HEVC (solid blue) and CCC (dashed red) cells as new: a) SOC range, b) cell skin temperature. The average current of the HEVC cycle is 3C ranging between 23C and 15C-rate, discharge and charge, respectively. (For interpretation of the references to color in this figure legend, the reader is referred to the web version of this article.)

the average temperature is lower due to the SOC adjustment procedure performed at lower currents (Fig. 1b). The two cycles have comparable average currents and power but significantly different SOC-ranges. A more detailed description on the cycles is found in previous work [38]. The CAL aged cell were stored between 48 and 43% SOC at a floating potential of 3.3 V and at 22 °C.

All cells were cycled in ambient temperature of 22 °C using a programmable Maccor® Series 4000 battery cell tester. Reference performance tests (RPT) including measurements of capacity, voltage profiles, energy and impedance/power during 10C-rate 18 s pulses (EUCAR test procedures) were performed at 22 °C approximately every two weeks throughout the test period. Additionally, an impedance spectrum at 50% SOC was performed using a Gamry® Reference 3000 potentiostat at every other RPT. Both HEVC and CCC conditions were controlled in a stepwise constant current mode with secondary limits set for voltages of 2 and 3.6 V.

Before disassembling the cells were fully discharged at 1C (CAL) or 1.3C rate (HEVC, CCC). The cells were opened and the jellyrolls were rolled up in a glove box (<1 ppm H_2O). For *post-mortem* analysis small samples were cut out at different locations of the jellyroll.

2.2. Electrochemical characterization of harvested electrodes

Electrode samples of 18 mm diameter were characterized electrochemically by capacity measurements and EIS. Since the electrode tapes are coated on both sides, the electrode coating on one side of the current collector was removed before cutting the samples by rubbing N-methyl-2-pyrrolidone (NMP) (Merck) with a cotton swab until reaching the current collector. Care was taken to prevent any NMP to touch the other side of the electrode. Two electrode samples from each specified location were prepared. The samples were rinsed in dimethyl carbonate (DMC) (SelectiLyte, Merck) and left to dry for 30 min before cell assembly, all performed in argon atmosphere (<1 ppm H_2O).

The capacity measurements were performed in a three-electrode set-up (EL-CELL, ECC-Ref) using lithium metal as counter and reference electrodes and a commercial electrolyte of 1 M $LiPF_6$ in 1:1 ethylene carbonate (EC): diethyl carbonate (DEC) (LP40, Merck). The working electrode and the lithium counter electrode were aligned and stacked in the electrochemical cell separated by three micro-fiber separators (Whatman GF/A) and placing the reference electrode in contact with the electrolyte midway between the electrodes. The position of the reference between the electrodes was adjusted with a Ti-spacer. Once assembled, the capacities of the electrodes were measured at low rates, 0.12–0.06 mA cm^{-2}, corresponding to roughly C/13. The capacity was measured between 0.002 and 1.5 V for graphite and 2.8–4.0 V for the $LiFePO_4$ electrodes. EIS were measured at a fixed SOC. For the negative graphite electrode, the EIS was measured at 127 mV vs. Li/Li$^+$ arriving from lithiated state. The positive $LiFePO_4$ electrode was set galvanostatically to 53% SOC based on the low-rate capacity measurement of the electrode. The EIS was then measured in a symmetrical set-up using the two collected samples, and the reported measurement is an average of the two samples. Electrode impedance was measured between 200 kHz and 5 mHz applying a 5 mV rms sinusoidal potential perturbation. Electrochemical measurements on electrode samples were performed using a Gamry PCI4/750 galvanostat/potentiostat.

2.3. Morphology and structure characterization

Both the positive and negative electrodes were investigated using Scanning Electron Microscopy (SEM). A Zeiss Sigma VP SEM with an accelerating voltage of 5 kV and pressure below 10^{-8} bar was used to study the appearance and morphology of the harvested electrodes. Energy dispersive X-ray spectroscopy (EDX) was performed using an Oxford instruments X-max 50. All samples were rinsed in DMC and kept under argon atmosphere before performing the SEM/EDX analysis. The samples were mounted onto sample holders and exposed to air for less than 10 min before analysis.

The surfaces of the graphite electrodes were analyzed with X-ray and hard X-ray photoelectron spectroscopy (XPS/HAXPES). Prior to the measurements the electrodes were washed with DMC except for the Fe2p measurements that were performed on both rinsed and non-rinsed samples. A PHI 5500 system with

monochromatized 1486.6 eV Al Kα radiation was used for the in-house XPS measurements. More bulk sensitive measurements were performed with synchrotron HAXPES at beam-line KMC-1 with the end station HIKE at the Helmholtz Zentrum BESSY II synchrotron (Berlin, Germany) with an excitation energy of 2300 eV. The relative intensities of the different peaks were determined using the detected core level peak areas and the Sco-field theoretical photoionization cross sections [43,44].

The LiFePO$_4$ electrodes were investigated using X-ray diffraction (XRD) in transmission geometry. The samples were vacuum-sealed into "coffee-bags" (polymer coated aluminum laminates), under argon atmosphere and examined by powder X-ray diffraction at the 711-beamline at the MAXIV laboratory synchrotron facility (Lund, Sweden), using an Oxford Diffraction Titan CCD detector. The beam size on the sample was about 1 mm^2. For the CCC and the HEVC samples a LaB$_6$ reference was used to refine the wavelength (1.11 Å) and the sample to detector distance was 123.8 mm. Diffraction patterns were collected with the detector at 0, 20, and 40° (covering 0–67° in 2θ). The powder pattern extraction tool in the CrysAlis-software was used to convert the collected data to stan-dard powder diffraction patterns. The CAL measurements were done with the detector at a fixed 0° position using a LaB$_6$ reference to refine the wavelength to 0.991 Å and the detector distance was calculated from the aluminum-foil content of the samples. Diffraction patterns were extracted with the Fit2d-software.

To calculate the weight fractions of LiFePO$_4$ and FePO$_4$ phases, Rietveld refinements of both phases were performed in a wide 2θ region (20.20–52.87) for HEVC and CCC, and (15.91–39.33) for CAL. Within these ranges some regions were excluded to cut away the diffraction peaks from the aluminum current collector and pack-aging material. Refinements were done in the Fullprof-software using the following procedure: polynomic background, wave-length, displacement parameter, and profile parameters were refined together with cell parameters and scale factors for both phases for a summation of the diffraction pattern for each series (CAL, CCC and HEVC). Cell parameters and profile parameters were then locked at their refined values and used as model to refine background polynomial, scale factors, wavelength and displace-ment factor in each diffraction pattern. From the calculated scale factors weight percentages were calculated.

3. Results

3.1. Full-cell cycling and aging

An overview of the performed aging sequences for the three cells is presented in Table 1, showing the cycling and storage pe-riods of the three cells, and the end capacity as measured with specified C-rate just prior to disassembly of the cells. Apart from cycling, there are storage periods of the HEVC and CCC cells ac-counting for the time between terminated cycling protocols and opening of the cells. The cells were disassembled at the same time leading to different storage times for the cycled cells.

Table 1
Overview of cell aging sequences for the three test conditions: HEVC, CCC, and CAL.

	HEVC	CCC	CAL
Start capacity/Ah	2.359	2.324	2.3[a]
Cycling period/days	439	70	—
Storage before opening/days	36	387	1026
Storage SOC	~90%	~90%	~42%
End discharge/C-rate	1.3 C-rate	1.3 C-rate	1 C-rate
End capacity/Ah	1.542	0.794	2.267
End capacity/% of Start cap.	65%	34%	99%

[a] Capacity as given by manufacturer.

The aging periods differ significantly between the aging sce-narios, as does the rate of performance degradation. As a bench-mark comparison, the 80% capacity retention (which is a common criterion for end-of-life) was reached after approximately 1400 equivalent 1C-cycles using the CCC procedure, but after 3700 under HEVC conditions. An equivalent 1C-cycle corresponds to 4.6 Ah. The cycle life (80% cap.) for the CCC procedure, though well in-line with specifications given by the supplier [45], is hence considerably lower than the cycle life obtained for the cell cycled according to HEVC conditions. As seen in Fig. 2, the CCC and HEVC cycling continued past 80% capacity retention before interrupted. On opening of the cells, the measured capacities were 65%, 34% and 99% of the start capacity for the HEVC, CCC, and CAL cases, respectively. At this time, the HEVC cell had cycled approximately 5400 capacity throughputs and the CCC only 2250 capacity throughputs while showing a much more pronounced capacity fade and impedance increase, demonstrating a larger detrimental effect of the CCC condition. However, the small variation in impedance in the first stage of cycling seen in Fig. 2b, shows that a cell aged under these conditions reaches a formal end-of-life (80% capacity retention) without suffering significant power loss.

The difference in impedance between the three cells measured prior to disassembly is also revealed in the EIS spectra in Fig. 2c and well in-line with the DC-measurements presented in Fig. 2b. For easier comparison, the inset table list the Re(Z) values for the different impedance contributions: the high frequency intercept (R_{hf}), the width of the mid-frequency semicircle (R_{sc}), the low frequency tail down to 10 mHz ($R_{tail,10mHz}$), and total real impedance (R_{tot}). Among
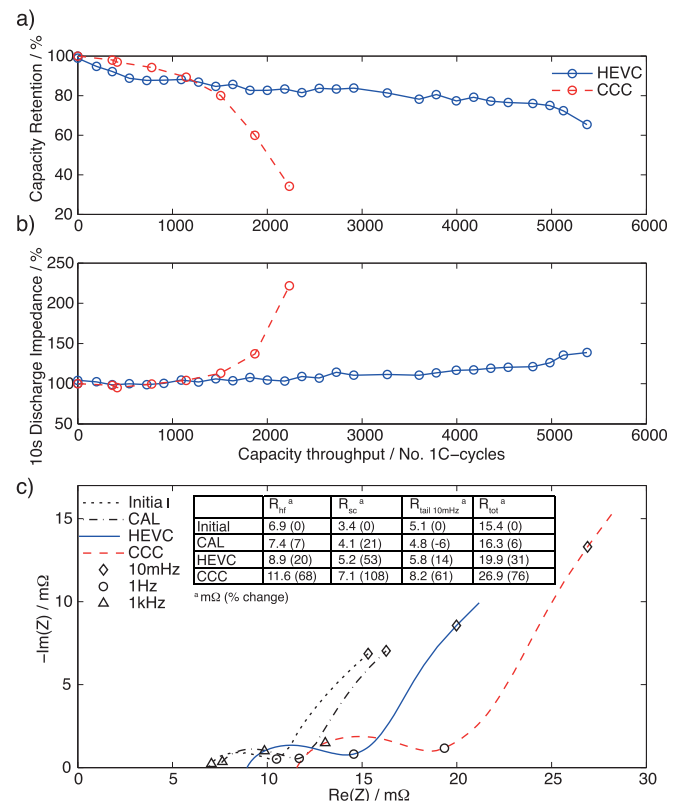

Fig. 2. Measurements of a) 1C discharge capacity retention, b) impedance after 10 s relaxation after 18 s 10C discharge pulse at 60% SOC for cells cycled according to the HEVC and CCC procedures, and c) EIS spectra at 22 °C ± 0.5 of new and aged cells (prior to disassembly of the cells). Inset table with Re(Z) impedance contributions from the high frequency intercept (R_{hf}), the width of the mid-frequency semicircle (R_{sc}), low frequency tail down to 10 mHz ($R_{tail,10mHz}$), and total real impedance (R_{tot}) in mΩ and % change.

the cells, the CCC shows largest increase for all listed impedance contributions, of which the R_{sc} has increased the most. The other cells also show the largest relative increase in R_{sc} compared to the other contributions, however only a small increase for the calendar-aged cell. A complete presentation of all test results from the reference tests and the EIS measurements is presented elsewhere [38].

3.2. Visual and morphological observations

Fig. 3 shows photographs of the electrodes from the newly opened cell. While the calendar-aged cell (CAL) shows homogenous and smooth electrode surfaces for both the negative and positive electrodes, the cycled graphite electrodes have a striking variation in appearance along the jellyroll. The skin parts, i.e. the outer part of the jellyroll lengthwise, of both cycled graphite electrodes are more homogenously dark to golden with some brighter areas (Fig. 3a, d). Halfway into the jellyroll of the HEVC graphite, a metallic appearance indicates deposition of metallic lithium, but bluish areas are also seen (Fig. 3b). Close to the core, the decreasing circumference of the roll gives the electrode a striped appearance. Differences are also observed across the width (marked Edge, Middle in Fig. 3) of the HEVC graphite tape; there are stripes along the edges, and effects from the tab on subsequent folds are visible. For the CCC cell, halfway into the jellyroll, the outer strip along the edge has a golden hue while the larger middle part has darker color, as shown in Fig. 3e, indicating that the outer strip is lithiated to a higher degree. Between these two areas a clear light edge of deposits is visible. Further, for the CCC case, some parts of the graphite electrode have detached from the current collector and have stuck to the separator. For all cells, while unrolling the innermost parts of the jellyroll, detachment from the copper current collector is apparent, since the graphite is brittle. Unlike the graphite electrodes, the positive LiFePO$_4$ electrodes appear uniform and similar for all cells, with a glossy appearance and no distinct visible deterioration.

For the remaining of this study, the overall focus of the *post-mortem* analysis is on two locations of the jellyroll: *Midpoint*—corresponding to the midpoint of the cell regarding both length and width dimension (Halfway Middle), and the outer extreme, *Edge*, which is the outer edge of both the length and width dimension (Skin Edge). Some of the characterization techniques presented below have also been applied to other parts of the tape, and are in that case indicated by the combination of length and width dimension, for example Core Edge.

A more detailed morphological comparison of the different electrodes using SEM is presented in Fig. 4. Comparing samples from the Midpoint and Edge locations of each cell, it is again the graphite that shows the largest differences due to cell usage and location in the jellyroll, while a similar appearance is found for all the LiFePO$_4$ electrode samples (the LiFePO$_4$ Edge samples are omitted with no visible variation from the other samples). The LiFePO$_4$ composite electrodes rather uniformly consist of nano-sized particles, displayed in Fig. 4c, f and i. For the graphite, the CAL cell has similar appearance at Midpoint and Edge areas, showing the graphite flakes comprising the electrode. In contrast, the CCC Midpoint, shown in Fig. 4d, has a thick deposited layer that, though cracked, covers the entire sample surface so that the underlying graphite flakes cannot be seen. However, at the CCC Edge location (Fig. 4e), the graphite flakes are clearly visible, but with a slightly granulated surface that is not seen at the CAL electrode. A comparison between the two locations of the HEVC electrode shows less variation than the same comparison for the CCC electrode. However, a more granulated surface can be distinguished on the Edge sample compared to the Midpoint, which is more similar to the morphology of the CAL graphite.

The apparently severe and spatially uneven degradation of the graphite electrode brought us to further investigate changes in its material properties and performance by electrochemical evaluation together with characterization using EDX, HAXPES and XPS as presented in the coming section. In addition, electrochemical evaluation and XRD measurements were performed on the LiFePO$_4$ electrodes in order to give input on full cell aging and possible SOC variations, concluding the Results section before the summarizing discussion in Section 4.

3.3. Properties of the graphite negative electrode

3.3.1. Electrochemical evaluation: capacity and EIS

To investigate variation in electrochemical performance, electrode capacity and EIS measurements were carried out on Midpoint and Edge locations selected from each cell. Fig. 5 shows the first delithiation (inset) and lithiation of harvested electrode samples at the different locations and duplicates from the same area, using a current of 0.12 mA cm^{-2} corresponding to about C/13 for the CAL aged electrode samples. The measurements were performed after re-assembling with an excess lithium source and fresh electrolyte. Keeping a low current, the measured capacity in this set-up hence
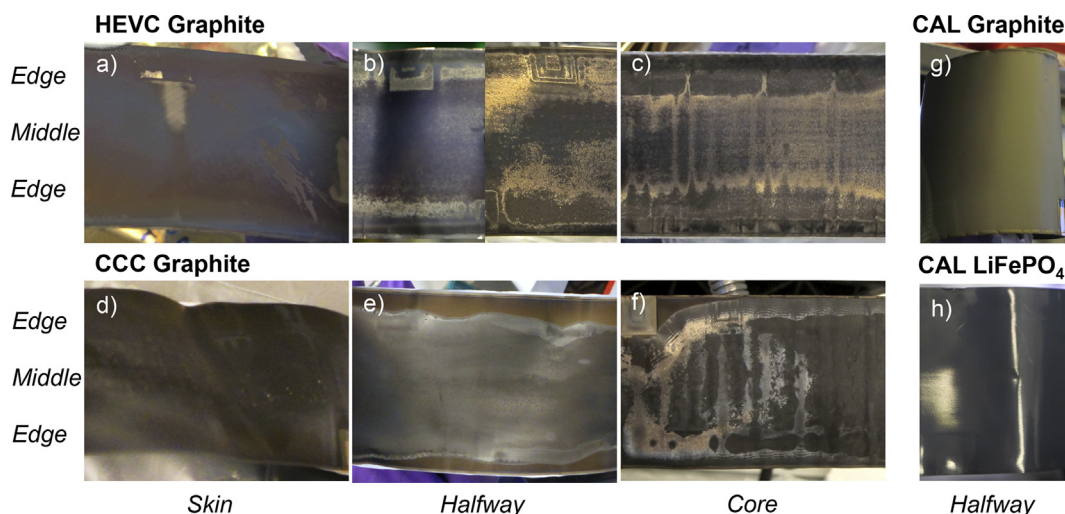

Fig. 3. Photographs of the negative electrodes of the disassembled cycled cells at Skin (a, d), Halfway (b, e), Core (c, f), and of the CAL aged negative (g) and positive (h) electrode at the Halfway location. The positive electrodes were visually similar for all opened cells.
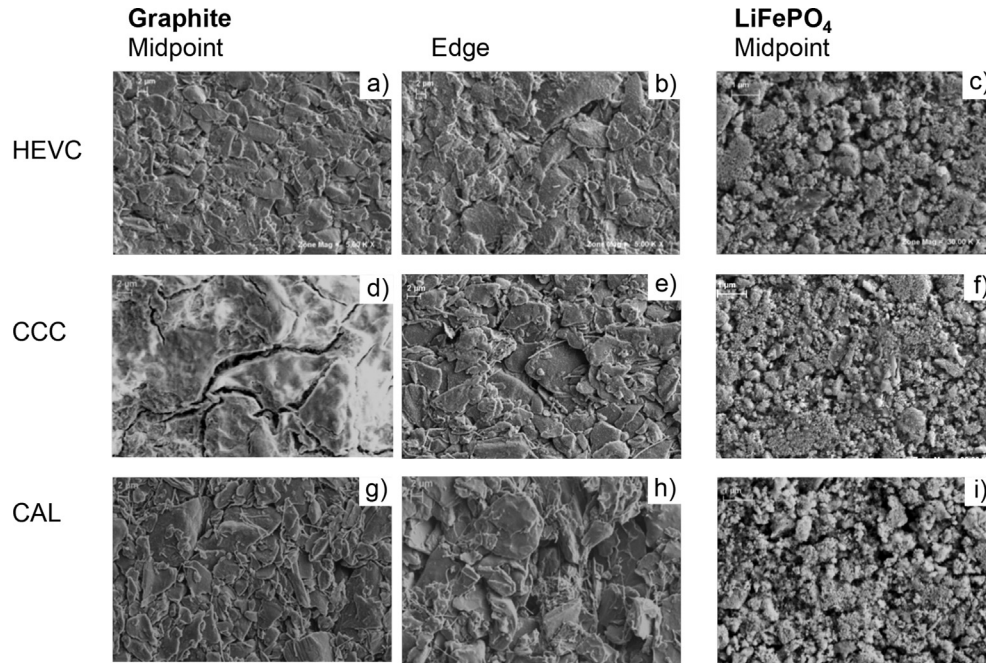
Graphite
Midpoint   Edge

LiFePO$_4$
Midpoint

Fig. 4. SEM images at 5 k magnification of aged graphite negative electrodes and at 30 k magnification of aged LiFePO$_4$ positive electrodes for HEVC (a–c), CCC (d–f), and CAL (g–i) cells, respectively.

reflects the available electrochemically active material in each electrode. In the inset it can be seen that all samples, except the CCC electrode at Edge location, initially were at low lithiation degree, as expected from discharging of the cells prior to disassembly. In contrast, the partly lithiated CCC Edge samples could be delithiated with approximately 0.27 mAh cm^{-2} compared to their capacity of 1.63 mAh cm^{-2}. The initial potential prior to first delithiation is also seen to vary.

Upon lithiation, the characteristic staging (degree of lithiation) of the graphite electrodes are clearly displayed for all samples. Some variation between the duplicate samples can be seen, especially for the CCC aged electrode, however, differences can be distinguished between aging scenario and location. The CAL electrodes show a negligible variation when comparing the Midpoint and Edge locations, and have suffered the least degradation on aging. For both cycled cells, however, there is a difference between sample locations. For the HEVC cell, the Midpoint discharge curves are similar to the CAL cell, while the Edge samples show a lower capacity, though no effect on polarization. The electrodes from the CCC cell have been the most affected by aging; especially the Midpoint samples have a considerable polarization and lower capacity than both the Edge location and the CAL and HEVC samples. The polarization is substantial considering the low C-rate of the discharge. The discharge capacities for the CCC Midpoint and the HEVC Edge sample stand out as having less electrochemically active material available than the other samples at the same low rate. For a better comparison of electrochemically active material available, the CCC samples were also measured at lower currents to correspond to the same C-rate of roughly C/13 but the lower current did not significantly increase the electrode capacity.

The EIS spectra of the electrodes are shown in Fig. 6, presented as a Nyquist and a Bode plot of −Im(Z) vs. frequency. The area specific impedance corresponds to the area of one electrode (18 mm diameter). Again, clear differences of electrode impedance depending on battery usage and location can be seen. The impedance is measured at approximately 50% SOC from 200 kHz to 5 mHz and, with an exception of the CCC Midpoint sample, the distinguishing features are two semicircles at high (>1 kHz) and mid frequencies (1 kHz–1 Hz), and a low frequency tail (<1 Hz). The high frequency resistance and coupled double layer (>1 kHz) have previously been assigned to the current collector [17,46–48]. In our experience, the graphite electrodes are somewhat brittle to handle, and therefore there is a risk that the attachment of the composite electrode to the current collector is affected by the sample preparation, i.e. when unrolling the electrodes, when removing the backside coating, and cutting out electrode samples from the electrode tape. High-frequency contact resistance variations are seen when handling the graphite samples, and current collector
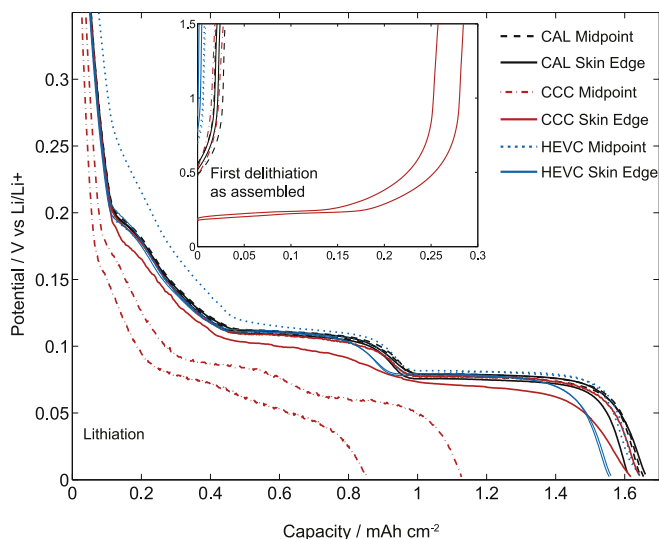

Fig. 5. Lithiation of the graphite electrode samples measured against a new lithium source using a constant current of 0.12 mA cm^{-1}. Insert: first delithiation on assembly.
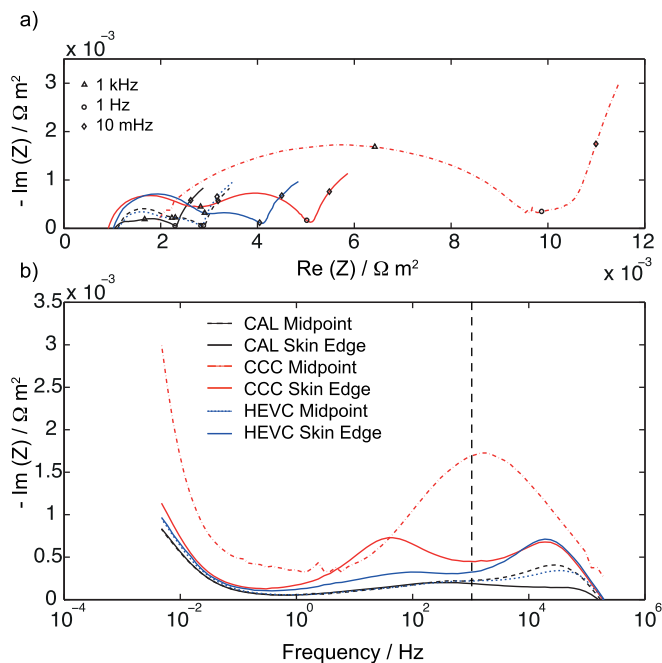
Fig. 6. Impedance spectra of graphite electrodes, CAL, CCC and HEVC, at locations Midpoint and Edge, a) Nyquist plot b) Bode plot. The vertical line marks 1 kHz. The area specific impedance corresponds to an electrode diameter of 18 mm.

Fig. 7. EDX spectra from the negative electrodes of the HEVC, CCC, and CAL aged cells.

resistances can therefore in this case not be assigned to electrode degradation from cycling or storage.

The mid-frequency semicircles of the samples in Fig. 6 vary in size, relating to interfacial properties of the porous electrode such as local resistances or surface changes of active materials affecting charge transfer resistances and double layers, or porosity decrease [17,49], which can all be affected by SEI growth. The CAL electrodes at both sample locations, and the HEVC samples at the Midpoint location are very similar, having the smallest mid-frequency impedance, indicating that the HEVC cycling has little effect on electrode degradation at the Midpoint. A 70% increase of the semicircle (real axis) is seen for the HEVC Edge electrodes compared to CAL Midpoint, and an increase of nearly 250% is seen for the CCC Edge samples. In contrast, the low-frequency resistances, $R_{tail\ 10mHz}$ (see Section 3.1), connected to ion transport in the electrolyte and active materials, have for these samples only increased with roughly 35% compared to CAL Midpoint. The impedance of the CCC Midpoint electrode sample is substantially larger than all other samples but varies in shape over the frequencies compared to the others. This is further investigated using a physics-based EIS model in an upcoming paper. This large performance loss is in agreement with the low capacity that was measured for these samples.

3.3.2. Composition of the graphite by EDX and XPS/HAXPES

The composition and character of surface layers formed on graphite were investigated using EDX, HAXPES, and XPS. HAXPES is a synchrotron based surface technique where a depth profiling through a surface can be obtained deeper into the bulk than conventional XPS [50,51]. For this the incoming photon energy can be varied and tuned from 2 to 12 keV.

Fig. 7 shows the EDX analysis of the graphite electrodes. The Cu current collector is detected for all samples, and this method can hence be considered a bulk method. Fluorine, phosphor and oxygen are also detected on all the samples, as can be expected for batteries using $LiPF_6$ based electrolytes in carbonate solvents [52]. However, the intensity of mentioned peaks varies in relation to the carbon
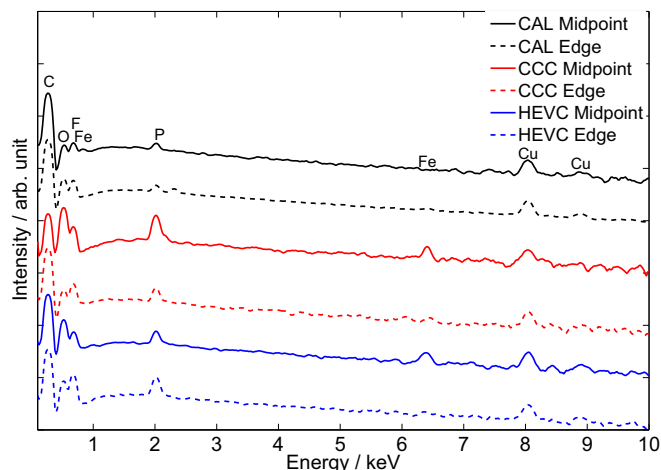
peak, indicating that there are different amounts of these species in each case. The probing depth of carbon is limited by its low energy emission, and varying thickness of surface layers can explain the relative carbon signal intensity. The spectrum of the CCC Midpoint sample shows the highest intensity of F, O and P compared to the intensity of C, thus indicating a thicker surface layer, and a significant peak assigned to Fe (at 6.4 keV) is also seen. The corresponding EDX measurements on the Edge sample show lower intensities of the peaks for F, O, and P compared to the intensity of C and no obvious Fe peak.

For the HEVC electrode, the Fe signal is present in the Midpoint spectrum but not in that of the Edge sample. This is similar to the CCC electrode and the relation between O and F at both locations is also similar to the corresponding locations of the CCC graphite. The intensities of F, O, and P are however not as high compared to the intensity of C. Finally, Midpoint and Edge samples from the CAL cell showed no trace of Fe and only small peaks for F, O, and P compared to C. Note that the F peak is overlapping with the Fe peak at ~0.7 keV (Fe Lα = 0.705 keV and F Kα = 0.677 keV) and this could result in a, by comparison, larger F-peak for the samples containing Fe.

For a detailed characterization of the surface film content and to estimate the SEI thickness, HAXPES was performed on the Midpoint location of the graphite electrodes as shown in Fig. 8. For the CAL-aged electrode, the peak for the carbon bulk material (at 282.3 eV) is visible in the C1s spectra, and can be used to estimate the SEI thickness. Taking into account that 95% of the signal comes from the top 18 nm of the surface, the graphite peak of less than one percent of the signal indicating a SEI thickness of more than 25 nm [44,53]. Comparing the other peaks, the surfaces of the cycled electrodes differ from the CAL aged electrode surface. The cycled graphite electrodes have higher relative intensity of compounds with C−O bonds (533.6 eV in O1s, 286.7 eV in C1s) and carbonates (531.9 eV in O1s, 290.1 eV in C1s) and lower relative intensities of compounds with P−F bonds (~136.8 eV in P2p 3/2). This is especially clear for the CCC aged electrode. The latter could be due to higher amounts of oxygenated $LiPF_6$ products (P−O/P=O features at 133.8 eV in P2p 3/2), which are formed in larger amounts on CCC and HEVC samples and are believed to form on cycling due to reactions of PF_5 with carbonates and/or alkoxides [22,53]. The relative intensity of lithium from the Li1s signal (not shown here) was found to be higher on the surface of the HEVC and CCC (23%) compared to the CAL sample (17%) and indicates loss of cyclable lithium in the SEI on cycling [36]. More LiF is seen on the CCC cycled electrode than the CAL stored ones, as indicated by the relation of the LiF peak to the P−F peak. The intensity of the F1 signal (relative
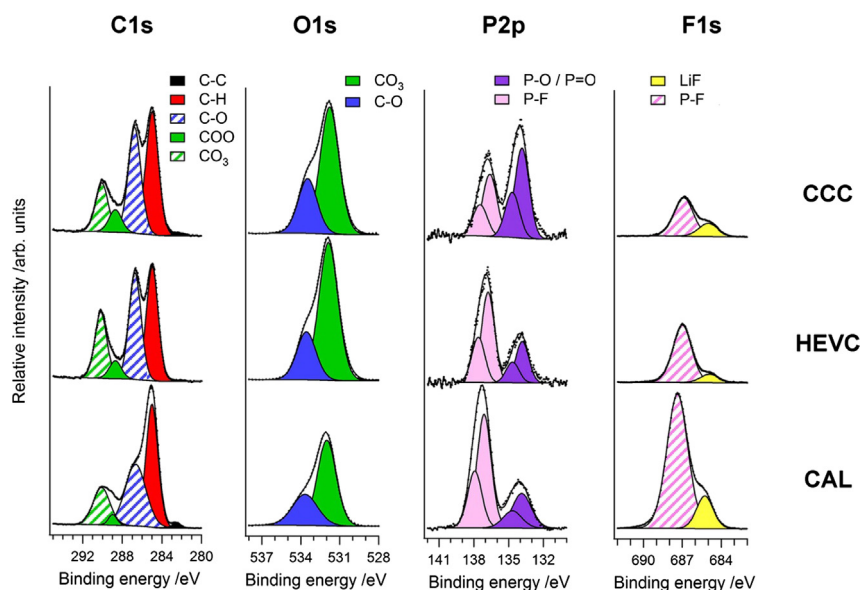
Fig. 8. C1s, O1s, F1s, and P2p HAXPES spectra of Midpoint graphite electrodes after the three different aging procedures (HEVC, CCC and CAL).

the sample signal) is, however, found to be largest for the CAL aged sample. The above results imply that the SEI on the cycled samples are thicker and contains more ethers, carbonates, lithium and features with P–O/P=O bonds than the stored electrode sample.

For the cycled cells, the Midpoint location was also compared to the Skin Middle location using conventional in-house XPS. The heterogeneous chemical character of the SEI [53,54] with both organic and inorganic compounds in a matrix makes it difficult to obtain a reliable relation between the different locations of the graphite electrodes. Except for the P2p and F1s compounds there are no clear trends. Fig. 9 shows the relative intensities of P–O (P2p), CO_3 (O1s), and LiF (F1s) signals within each sample. The variations between different locations within the electrodes are in the same magnitude as between different aging conditions. The LiF and CO_3 peak intensities are overall stronger for the CCC cycled electrode than for the HEVC electrode but lower for P–O. However, higher intensities of fluoride species are found at the Skin Middle than at the Midpoint samples, while the opposite is observed for the carbonate species for both CCC and HEVC electrode.

XPS was also employed in order to investigate the presence of iron in the SEI layer on the surface of the graphite negative electrode. A weak Fe2p 3/2 peak was only detected for the CCC samples and the intensity is higher for unwashed than washed samples. Due to the overlap of the Fe 2p core level peak with the fluorine plasmon it was

difficult to quantify the amount of Fe. The deviation between XPS and EDX detection of iron could be due to different penetration depths.

3.4. Properties and utilization of the LiFePO₄ positive electrode

3.4.1. Electrochemical evaluation: capacity and EIS

Fig. 10 displays the discharge capacities of the $LiFePO_4$ electrode samples at the Midpoint location for two current densities, 0.12 mA cm^{-2} and 1.2 mA cm^{-2} (ca. C/13.5 and C/1.35, respectively). From the first delithiation of the electrodes as assembled (Insert Fig. 10), a lower lithiation degree for the CCC sample compared to CAL and HEVC samples can be seen. A first comparison between the positive and negative electrodes' discharge capacities shows that the variation in aging is smaller for the $LiFePO_4$ electrode between the three aging conditions. The capacity for the CCC sample is slightly smaller than the other $LiFePO_4$ electrodes and at higher discharge rates some polarization is observed, indicating higher resistance.
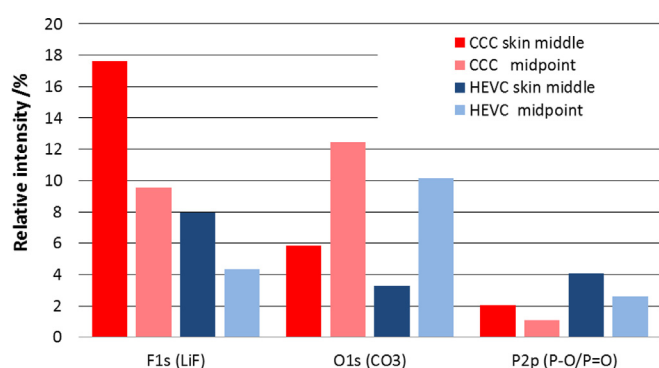

Fig. 9. Relative intensities of O1s, P2p (P–O species) and F1s detected components for HEVC and CCC: comparison of Skin Middle and Midpoint regions.
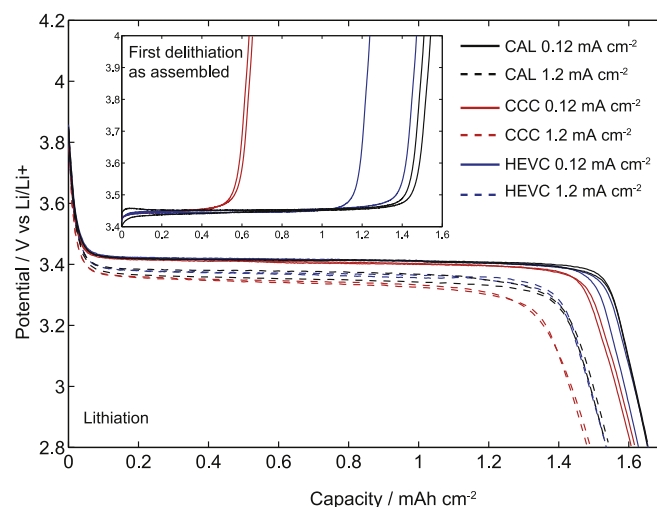

Fig. 10. Lithiation of LiFePO₄ at currents of 0.12 and 1.2 mA cm⁻² at the Midpoint location of the jellyroll. Inset: First delithiation, 0.12 mA cm⁻².

The impedance spectra of Midpoint samples are shown in Fig. 11. In the mid frequency region (1 kHz–1 Hz) the impedance is minor for all electrode samples, which could be an effect of the small particle sizes, resulting in small local current densities. Their similarity indicates small changes in performance due to degradation within the bulk of the electrode. The high frequency resistance (>1 kHz) is, however, seen to vary between the aged electrodes. The non-depressed shape of the high frequency semicircle indicates a process that is not distributed within a porous structure, and the current collector is proposed to cause the semicircle. Even though the differences between electrodes are small compared to the graphite electrode, the measurements show least impedance for the HEVC sample.

One way to visualize the usage of the two electrodes in full cell is to calculate a theoretical SOC-window [12,13]. The relative slippage between the two capacity curves is approximated from the lithiation degrees given from the first-lithiation (inset Figs. 5 and 10) relative the electrode capacity (Figs. 5 and 10). From the SOC-window any mismatch between the electrodes as a result of for example loss of cyclable lithium or material degradation can be estimated. Fig. 12 shows an overview of electrode matching of the Midpoint samples of each cell. The Edge location of the CCC case is also shown, since the graphite electrode had an unexpectedly high degree of lithiation. The theoretical SOC window is marked as a light red area. The dashed vertical line through the curves shows at which states the electrodes were when the cells were opened.

For all samples presented (Fig. 12) it can be seen that the graphite electrode limits the theoretical SOC window at completely discharged state and the LiFePO$_4$ electrode at completely charged state. For the cycled cells, especially for the CCC Midpoint sample, the graphite curve is shifted to the left in relation to the LiFePO$_4$ curve, resulting in a smaller SOC window. A shift in this direction is in general indicative of loss of cyclable lithium in reduction reactions [55], which is hence substantial for the CCC samples and less for HEVC Midpoint, but still noticeable. The SOC window for the CCC Midpoint is approximately 45% of the SOC window of the CAL Midpoint.
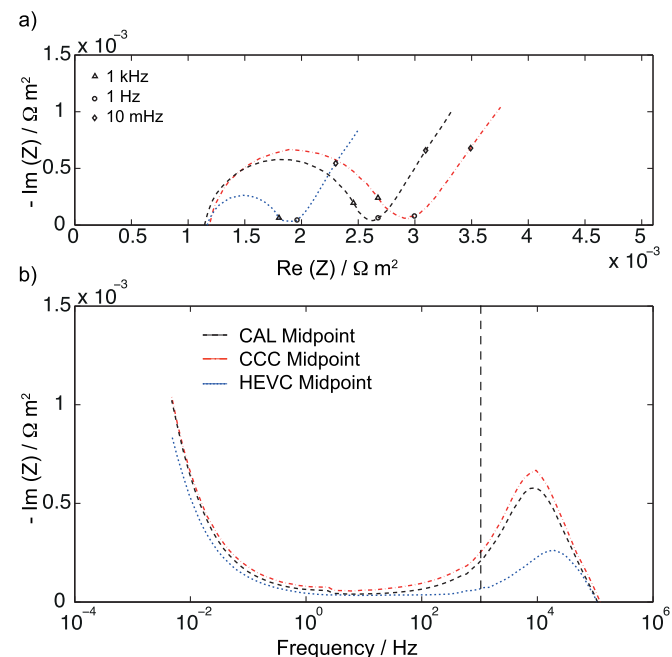

Fig. 11. EIS of LiFePO$_4$ at Midpoints of aged electrodes, a) Nyquist representation, b) Bode-plot. The vertical line marks the 1 kHz frequency.
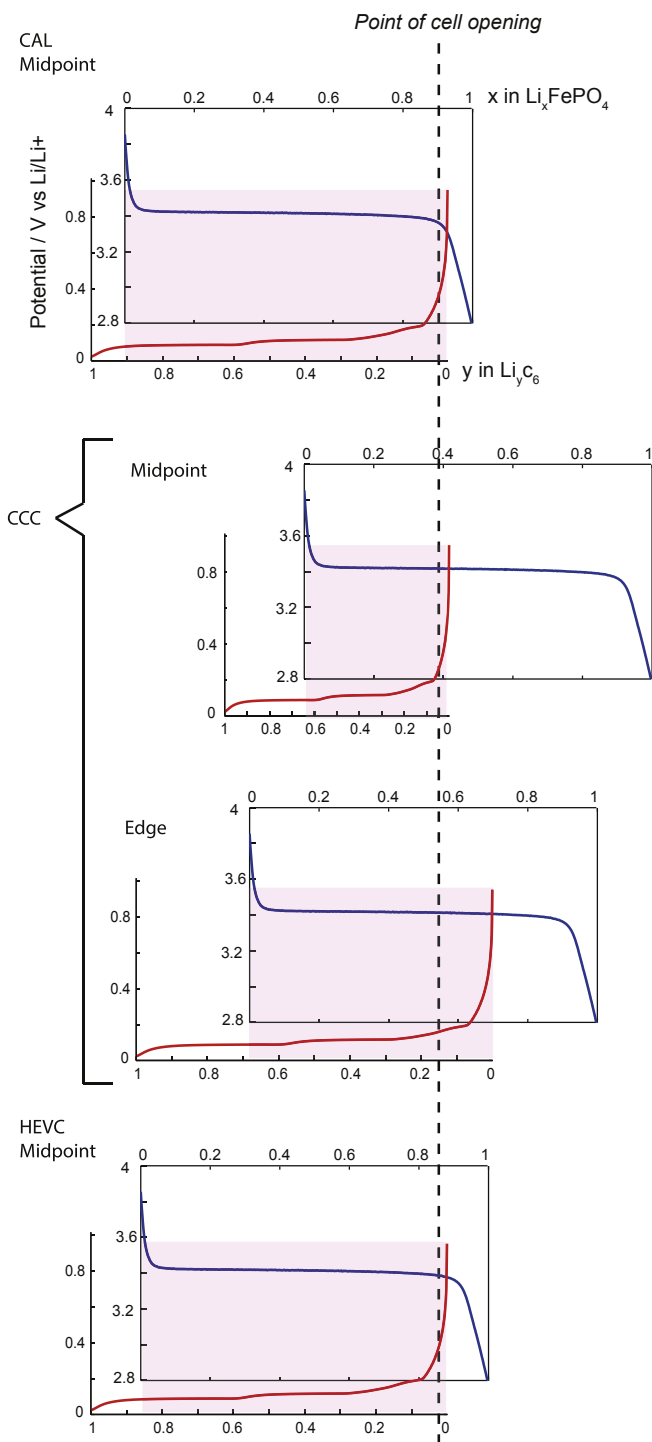

Fig. 12. Electrode matching of probed cells from capacity measurements on electrode samples.

Since there were low amounts of lithium in all graphite samples upon opening (inset Fig. 5), with an exception for the CCC Edge location, the amount of lithium in the LiFePO$_4$ electrode could hence also be used as an approximation of the relative electrode shift.

3.4.2. Bulk composition by XRD

An accurate determination of the degree of lithiation can be obtained using XRD and Rietveld refinement from the relative

amounts of LiFePO$_4$ and FePO$_4$. Between the d-spacings^{-1} 0.321 Å^{-1} and 0.375 Å^{-1} LiFePO$_4$ has two diffraction peaks found at 0.331 Å^{-1} and 0.358 Å^{-1}, and FePO$_4$ has three peaks at 0.338 Å^{-1}, 0.345 Å^{-1}, and 0.368 Å^{-1}. In addition to the electrochemically investigated Midpoints, a larger number of locations from the LiFePO$_4$ electrodes were investigated by synchrotron XRD, shown in Fig. 13.

The XRD results show that, with the exception for HEVC Midpoint, all samples contain FePO$_4$ to some extent. The CAL electrode has a uniform and high degree (∼90%) of lithiation through the whole cell. In contrast, both the CCC and HEVC electrodes have lower degrees of lithiation in comparison to the CAL scenario, and are also not as uniform across the jellyroll displaying mixed phases over the entire electrode with lower lithiation degrees towards the core of the jellyroll. The HEVC is found to have the largest differences in lithiation between different locations of the electrode tape, with the highest lithiation degree at Midpoint and lower both further into the core and towards the skin. The

calculated LiFePO$_4$ weight fractions compares well to the electrochemical measured data and coincide with the intercept of the dashed vertical line and the LiFePO$_4$ lithiation curve for a given point in Fig. 12. The XRD measuring points spread out over the entire electrode tape then gives an overview of the utilization of cell material.

4. Discussion

From the presented results several conclusions can be made regarding battery aging as a result of the different usage patterns. In agreement with previous studies [13,17,22] calendar aging at room temperature does not result in significant degradation of the electrode or cell performance. As expected, it is also evident from full cell monitoring that constant current cycling in a broad SOC range is, in the long run, considerably more detrimental to the battery than a hybrid electrical vehicle cycle. In this study, the most striking results are, however, the inhomogeneous properties of the probed cycled electrodes as a function of location in the cylindrical cell design. The variation in properties indicate that the distributions of current/temperature over the wound cells during cycling can precipitate into spatial distributions of electrode degradation and decomposition reactions, leading to unevenly distributed aging. This non-homogeneity created within the cell can be one explanation to the path dependent aging in lithium-ion batteries as the order in which short time usage conditions (power pulses) are applied to the cell will influence local temperature and current distributions determining where in the cell the redox-chemistry will take place. Our observations for the cycled cells are discussed and summarized below.

4.1. Constant current aging

Constant current cycling in a large SOC window results in a fast degradation of cell capacity. This loss in performance is mainly associated with an uneven and significant degradation of the graphite electrode and loss of cyclable lithium. The pronounced electrode mismatch seen at the Midpoint (Fig. 12) is related to loss of cyclable lithium from reduction of electrolyte components on the graphite surface in forming the SEI, and is in agreement with the thick surface layer at the Midpoint revealed by SEM. Accordingly, the intensities for O, P, and F are high in comparison to the carbon content. Furthermore, the cycling induces higher relative amounts of ethers, carbonates, lithium, and features with P−O/P=O. Sustained degradation of the graphite electrode with substantially larger electrode-impedance and loss of electrochemically active material was observed. However, whether the high impedance is associated with the surface composition of the SEI or its physical properties are difficult to establish. EDX and XPS show Fe contamination in the graphite electrode by Fe dissolution from the LiFePO$_4$ electrode, known to occur using LiPF$_6$ containing electrolytes at elevated temperatures [56,57]. Iron present in the graphite electrode has been reported to increase electrode impedance by accelerating film formation [16,58].

The analysis of the graphite Edge samples regarding performance, morphology (SEM), and film composition (EDX) all indicate less electrode degradation compared to the Midpoint of the cell but more degraded than the CAL aged graphite. The theoretical SOC window also implies that a larger part of both electrodes can be utilized compared to Midpoint. At the Edge, there is a deviation between the dashed line (Fig. 12) and the fully delithiated graphite of the SOC window. This could represent an increased local polarization at this point since the cell is discharged to a cut-off voltage. Since the graphite electrode performance is better at this location than at the Midpoint, it could be an effect of locally increased
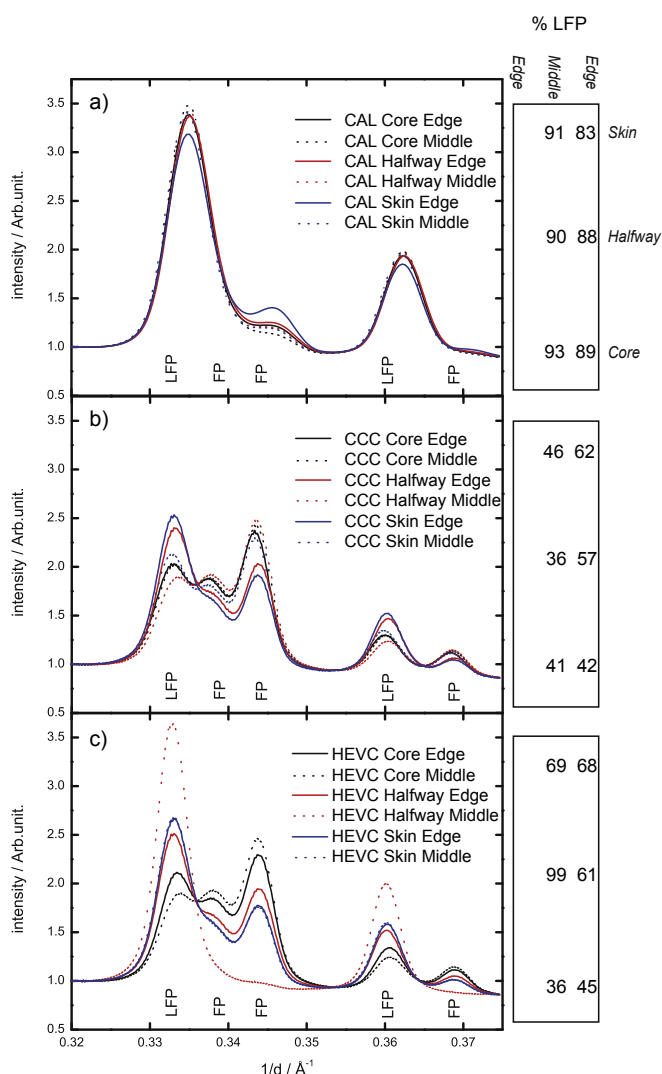

Fig. 13. Synchrotron X-ray diffraction patterns for a) CAL, b) CCC, and c) HEVC aged LiFePO$_4$ and to the right schematic picture of jellyroll with calculated weight fractions of LiFePO$_4$ as determined from Rietveld refinements (all standard deviations as calculated in the refinements were less then 0.5%). Both edge (solid line) and middle (dotted line) of the electrode coil were examined at core (black), halfway (red) and skin (blue) positions. Indicated in all subfigures are also the expected peak positions for LiFePO$_4$ (LFP) and FePO$_4$ (FP). (For interpretation of the references to color in this figure legend, the reader is referred to the web version of this article.)

current density possibly affected by the high impedance at the Midpoint forcing higher current densities at the Edge, during the final discharge. Effects of unevenly distributed electrolyte are difficult to take into account when disassembling the cell, but several samples from the same area gave similar results. Also effects from tab locations are expected to influence potential distributions, but were not investigated clearly in this study.

In comparison to the graphite electrode, the $LiFePO_4$ electrode material appears unaffected by cycling, with no distinct differences in appearance by SEM or electrochemical performance. This is in contrast to our previous study on small lab-scale cells [17] where both cracking and lowered electrode porosity could be distinguished on the $LiFePO_4$ electrode. The deviation could be explained by differences in cell manufacturing, the smaller particle size and any non-specified electrolyte additives that usually are present in the commercial cells. However, the iron found on the graphite electrode by EDX indirectly indicates some aging of the $LiFePO_4$ electrode and is suggested to be an effect of the higher temperatures further into the jellyroll, since iron only was detected at Midpoints of both cycled cells. The good performance of the $LiFePO_4$ electrodes in half-cell measurements suggests that the uneven degree of lithiation, as measured by XRD, is more likely an effect of mismatch between positive and negative electrodes and uneven battery utilization rather than an inhomogeneous degradation of the electrode itself. It should be noted that, before the full-cell discharge preceding cell disassembly, the cells had been left at open circuit and room temperature. The uneven degrees of lithiation by XRD are hence not a temporal effect of temperature distributions present in the cells while cycling, but a sustained effect.

Returning to the full cell behavior in the CCC scenario, the overall cell capacity is critically decreased already after a relatively short time of cycling and is, after further cycling, followed by an increase of the impedance. Considering above reasoning, one hypothesis is that the initial capacity loss correlates to loss of cyclable lithium, occurring preferentially though not exclusively towards the inner part of the cell. This would lower the capacity but not necessarily affect the cell impedance. As more and more of the graphite active material in the inner parts of the cell is lost, and covered with increasingly resistive surface films, a smaller part of the cell can be used, leading to a higher overall cell resistance. Nevertheless, R_{sc} (Fig. 2) has a larger relative contribution to the total impedance increase, and with only minor impedance variation of the positive electrode in this frequency range (1 kHz-1 Hz), this likely correlates to the negative electrode degradation as discussed above.

4.2. HEVC aging

The HEVC cycled cell is overall found to be less degraded than the CCC cell despite being cycled for a longer time, as is evident from the full cell measurements. Lithium plating was observed in the photographs in accordance to a small voltage plateau at high SOC in the discharge curve of the full cell shown elsewhere [38]. In contrast to the CCC case, the analysis shows that the Midpoint graphite samples are similar to the CAL electrodes regarding electrochemical performance and SEM observations and it has relatively low P, O, and F to C ratios compared to the corresponding CCC samples according to EDX. Nevertheless, Fe was also detected at Midpoint indicating that impedance increase seen for the CCC graphite electrode is not only correlated to the presence of iron, but also to other aspects of the cycling. The relative electrode shifts shown in Fig. 12 also shows a much smaller loss of cyclable lithium at the Midpoint location compared to the CCC aged cell, but still a slightly smaller available SOC window compared to the CAL aged cell.

The analysis of the graphite Edge location shows that it is more degraded than the Midpoint, having lower capacity, more rugged surface appearance and slightly higher impedance, though no Fe is detected. Lower degrees of lithiation were found by XRD at the $LiFePO_4$ electrode skin locations compared to the Midpoint indicating more loss of cyclable lithium at the Edge than Midpoint, in contrast to the CCC case.

From this study it is speculative to say whether the HEVC ages the cells differently or just more slowly than CCC. Our comparison of the degradation of HEVC and CCC cells suggests that the large SOC-range is more detrimental than both current rates and temperature during cycling. This is something to take into account when sizing the battery system properly for a given application since reducing the size could give additional costs considering that a smaller battery would mean a larger SOC-range needed, which then can result in a shorter battery life.

The different patterns of non-uniform degradation reflect the complexity of degradation in commercial cells by different cycling schemes. It should be noted that the analysis of the few locations investigated in this study points at significant differences in aging along the electrode tapes for cycled cylindrical cells but is unable to show the full picture. Further investigations are needed to track the distribution of degradation within the cell with a larger number of locations, also taking the tab positions into account. However, for a better understanding of battery aging, complementary investigations on controlled model systems that simulate the different conditions that may arise in a larger cell concerning for instance pressure and temperature, are needed in order to interpret the signs of aging in commercial cells for use in vehicles.

5. Conclusion

In this study commercial $LiFePO_4$//graphite 2.3 Ah cylindrical cells, optimized for power applications, were aged at three different conditions at $+22\ ^\circ C$: (i) simulated hybrid electric vehicle bus cycle within a narrow SOC-range, (ii) constant current mode over a 90% SOC-range and (iii) calendar aged during approximately three years. After full-cell performance characterization, the cells were disassembled, and *post-mortem* analyses were performed at different locations along the jellyroll by electrochemical half-cell capacity and impedance measurements, microscopy (SEM/EDX) and electrode analysis by synchrotron XRD and HAXPES and in-house XPS.

The results show that both cycled cells displayed uneven aging within the cell electrodes, i.e. large differences were found in electrode properties in the Midpoint of the cell coil compared to the Edges, whereas the electrodes of the calendar aged cell was uniform and not significantly affected by aging. The aging variations within the cycled cells were identified as different capacity and impedance of the graphite electrode, associated with different SEI thicknesses and compositions, and loss of cyclable lithium, which was mirrored by a varying degree of lithiation in the positive electrode and electrode matching. The most degraded cell, cycled at constant current conditions, was characterized by a thick deposited layer on the negative electrode at Midpoint that severely decreased the performance, while the hybrid cycled graphite electrode, despite apparent lithium plating, showed slight performance degradation at its corresponding parts. In both cycled cells, iron dissolved from the positive electrode was detected on the Midpoint of the negative. Otherwise, the performance of the cycled positive $LiFePO_4$ electrodes in half-cell measurements were comparably high, which strongly suggest that the low and unexpectedly varying degree of lithiation of the harvested electrodes is a consequence of decreased utilization of the positive electrodes, due to local miss-matching with the facing graphite electrodes, correlated to loss of

cyclable lithium. It is argued that gradients in temperature and pressure, and positions of the tabs within a cylindrical cell, can give rise to current density and potential distributions within the jellyroll during cycling, that result in the sustained spatial variation in electrode degradation and utilization observed.

The implications of uneven aging are an important issue for cylindrical cells. For example, uneven utilization of the active cell materials creates an unnecessary need to over-dimension battery systems to meet specific requirements for a given application. Further, an uneven aging complicates the development of state-of-health SOH-estimations and predictions, due to a large combination of different internal aging processes, which can result in the same effect on performance degradation on cell or pack level. The uneven utilization indicated in this study, likely caused by temperature gradients within the cell, emphasize the importance of choosing a suitable cell format and design, and cooling strategy to obtain long-lasting battery solutions for heavy-duty HEV applications.

Acknowledgment

References

[1] Japanese Government Incentive for the Purchase of Environmentally Friendly Vehicles, Japan Automobile Manufacturers Association Inc., Tokyo, 2009.
[2] E. Jobson, in: Hybrid Technology for Buses: European Fleets Conference, Örebro, Sweden, 2010.
[3] Mercedes-Benz, (Ed.), 2014, http://www5.mercedes-benz.com/en/vehicles/trucks/the_atego_bluetec_hybrid/.
[4] M. Anderman, Assessing the Future of Hybrid and Electric Vehicles, 2013. The 2014 xEV Industry Insider Report, http://www.advancedautobat.com.
[5] O.P.R. van Vliet, T. Kruithof, W.C. Turkenburg, A.P.C. Faaij, J. Power Sources 195 (2010) 6570–6585.
[6] M. Grahn, C. Azar, M.I. Williander, J.E. Anderson, S.A. Mueller, T.J. Wallington, Environ. Sci. Technol. 43 (2009) 3365–3371.
[7] H. Joachin, T.D. Kaun, K. Zaghib, J. Prakash, J. Electrochem. Soc. 156 (2009) A401–A406.
[8] Batteries for Sustainability: Selected Entries from the Encyclopedia of Sustainability Science and Technology, Springer New York, New York, NY, 2013.
[9] B. Scrosati, J. Garche, J. Power Sources 195 (2010) 2419–2430.
[10] B.Y. Liaw, M. Dubarry, J. Power Sources 174 (2007) 76–88.
[11] M. Kassem, J. Bernard, R. Revel, S. Pelissier, F. Duclaud, C. Delacourt, J. Power Sources 208 (2012) 296–305.
[12] M. Kassem, C. Delacourt, J. Power Sources 235 (2013) 159–171.
[13] M. Safari, C. Delacourt, J. Electrochem. Soc. 158 (2011) A1123–A1135.
[14] M. Dubarry, B.Y. Liaw, J. Power Sources 194 (2009) 541–549.
[15] P. Liu, J. Wang, J. Hicks-Garner, E. Sherman, S. Soukiazian, M. Verbrugge, H. Tataria, J. Musser, P. Finamore, J. Electrochem. Soc. 157 (2010) A499–A507.
[16] K. Amine, J. Liu, I. Belharouak, Electrochem. Commun. 7 (2005) 669–673.
[17] T.G. Zavalis, M. Klett, M.H. Kjell, M. Behm, R.W. Lindström, G. Lindbergh, Electrochim. Acta 110 (2013) 335–348.
[18] S.C. Nagpure, R. Dinwiddie, S.S. Babu, G. Rizzoni, B. Bhushan, T. Frech, J. Power Sources 195 (2010) 872–876.
[19] S.C. Nagpure, B. Bhushan, S.S. Babu, J. Electrochem. Soc. 160 (2013) A2111–A2154.
[20] S.C. Nagpure, B. Bhushan, S. Babu, G. Rizzoni, Scr. Mater. 60 (2009) 933–936.
[21] M. Kerlau, M. Marcinek, V. Srinivasan, R.M. Kostecki, Electrochim. Acta 52 (2007) 5422–5429.
[22] M.H. Kjell, S. Malmgren, K. Ciosek, M. Behm, K. Edstrom, G. Lindbergh, J. Power Sources 243 (2013) 290–298.
[23] T.M. Bandhauer, S. Garimella, T.F. Fuller, J. Electrochem. Soc. 158 (2011) R1–R25.
[24] M. Fleckenstein, O. Bohlen, M.A. Roscher, B. Baker, J. Power Sources 196 (2011) 4769–4778.
[25] K. Somasundaram, E. Birgersson, A.S. Mujumdar, J. Power Sources 203 (2012) 84–96.
[26] G.S. Zhang, C.E. Shaffer, C.Y. Wang, C.D. Rahn, J. Electrochem. Soc. 160 (2013) A610–A615.
[27] U.S. Kim, C.B. Shin, C.-S. Kim, J. Power Sources 180 (2008) 909–916.
[28] D.P. Abraham, J.L. Knuth, D.W. Dees, I. Bloom, J.P. Christophersen, J. Power Sources 170 (2007) 465–475.
[29] D. Aurbach, B. Markovsky, A. Rodkin, M. Cojocaru, E. Levi, H.J. Kim, Electrochim. Acta 47 (2002).
[30] D.P. Abraham, J. Liu, C.H. Chen, Y.E. Hyung, M. Stoll, N. Elsen, S. MacLaren, R. Twesten, R. Haasch, E. Sammann, I. Petrov, K. Amine, G. Henriksen, J. Power Sources 119 (2003).
[31] M. Dubarry, B.Y. Liaw, M.-S. Chen, S.-S. Chyan, K.-C. Han, W.-T. Sie, S.-H. Wu, J. Power Sources 196 (2011) 3420–3425.
[32] M. Dubarry, C. Truchot, B.Y. Liaw, J. Power Sources 219 (2012) 204–216.
[33] I. Bloom, A.N. Jansen, D.P. Abraham, J. Knuth, S.A. Jones, V.S. Battaglia, G.L. Henriksen, J. Power Sources 139 (2005) 295–303.
[34] Y. Zhang, C.-Y. Wang, X. Tang, J. Power Sources 196 (2011) 1513–1520.
[35] M. Broussely, P. Biensan, F. Bonhomme, P. Blanchard, S. Herreyre, K. Nechev, R.J. Staniewicz, J. Power Sources 146 (2005) 90–96.
[36] J. Vetter, P. Novak, M.R. Wagner, C. Veit, K.C. Moller, J.O. Besenhard, M. Winter, M. Wohlfahrt-Mehrens, C. Vogler, A. Hammouche, J. Power Sources 147 (2005) 269–281.
[37] B. Markovsky, A. Rodkin, Y.S. Cohen, O. Palchik, E. Levi, D. Aurbach, H.J. Kim, M. Schmidt, J. Power Sources 119–121 (2003) 504–510.
[38] J. Groot, Licentiate thesis, Chalmers University of Technology, 2012, p. 146.
[39] F. Savoye, P. Venet, M. Millet, J. Groot, Ind. Electron., IEEE Trans. 59 (2012) 3481–3488.
[40] I. Bloom, B.W. Cole, J.J. Sohn, S.A. Jones, E.G. Polzin, V.S. Battaglia, G.L. Henriksen, C. Motloch, R. Richardson, T. Unkelhaeuser, D. Ingersoll, H.L. Case, J. Power Sources 101 (2001) 238–247.
[41] J. Li, E. Murphy, J. Winnick, P.A. Kohl, J. Power Sources 102 (2001) 294–301.
[42] J. Groot, in: International Battery, Hybrid and Fuel Cell Electric Vehicle Symposium (EVS-24), 2009, p. 3050179. Stavanger, Norway.
[43] J.H. Scofield, in: Other Information: UNCL. Orig. Receipt Date: 30-JUN-73, 1973, pp. Medium: ED; Size: Pages: 376.
[44] K.C. Hogstrom, S. Malmgren, M. Hahlin, H. Rensmo, F. Thebault, P. Johansson, K. Edstrom, J. Phys. Chem. C 117 (2013) 23476–23486.
[45] A123 ANR26650M1A battery data sheet, http://www.a123rc.com/goods-101-Nano-Phosphate+LiFePO4+Original+A123+ANR26650M1A+Cell.html
[46] M. Gaberscek, J. Moskon, B. Erjavec, R. Dominko, J. Jamnik, Electrochem. Solid State Lett. 11 (2008) A170–A174.
[47] R. Petibon, C.P. Aiken, N.N. Sinha, J.C. Burns, H. Ye, C.M. VanElzen, G. Jain, S. Trussler, J.R. Dahn, J. Electrochem. Soc. 160 (2013) A117–A124.
[48] A.K. Hjelm, G. Lindbergh, Electrochim. Acta 47 (2002).
[49] D. Dees, E. Gunen, D. Abraham, A. Jansen, J. Prakash, J. Electrochem. Soc. 152 (2005) A1409–A1417.
[50] M. Gorgoi, S. Svensson, F. Schaefers, W. Braun, W. Eberhardt, Eur. Phys. J.-Spec. Top. 169 (2009) 221–225.
[51] B. Philippe, R. Dedryvere, J. Allouche, F. Lindgren, M. Gorgoi, H. Rensmo, D. Gonbeau, K. Edstrom, Chem. Mater. 24 (2012) 1107–1115.
[52] M. Nie, D. Chalasani, D.P. Abraham, Y. Chen, A. Bose, B.L. Lucht, J. Phys. Chem. C 117 (2013) 1257–1267.
[53] S. Malmgren, K. Ciosek, M. Hahlin, T. Gustafsson, M. Gorgoi, H. Rensmo, K. Edstrom, Electrochim. Acta 97 (2013) 23–32.
[54] A.M. Andersson, K. Edstrom, J. Electrochem. Soc. 148 (2001) A1100–A1109.
[55] J. Christensen, J. Newman, J. Electrochem. Soc. 152 (2005) A818–A829.
[56] M. Koltypin, D. Aurbach, L. Nazar, B. Ellis, J. Power Sources 174 (2007) 1241–1250.
[57] N. Dupre, J.F. Martin, J. Degryse, V. Fernandez, P. Soudan, D. Guyomard, J. Power Sources 195 (2010) 7415–7425.
[58] K. Striebel, J. Shim, A. Sierra, H. Yang, X.Y. Song, R. Kostecki, K. McCarthy, J. Power Sources 146 (2005).